Effects of Microphysical Processes on the Precipitation Spectrum in a Strongly Forced Environment

Jin-De Huang[1] and Chien-Ming Wu[1]

[1]Department of atmospheric sciences, National Taiwan University, Taipei, Taiwan

Corresponding author: Chien-Ming Wu (mog@as.ntu.edu.tw)

Key Points:

- The predicted particle properties (P3) microphysics scheme is formally implemented in a vector vorticity equation cloud-resolving model (VVM).
- The P3 scheme exhibits stronger extreme precipitation under a strongly forced environment compared to the original scheme.
- The reduced melting effects associated with strong convective updrafts in P3 can result in more extreme precipitation.

Abstract

This study investigates the effects of microphysical processes on the precipitation spectrum in a strongly forced environment using a vector vorticity cloud-resolving model (VVM). Experiments are performed under imposed advective cooling and moistening with two microphysics parameterizations: predicted particle properties scheme (P3) and Lin scheme (VVM-Lin). Even though the domain-averaged precipitation is similar in two experiments, P3 exhibits stronger extreme precipitation in the spectrum compared with VVM-Lin. Changes in convective structures are responsible for such a difference. Using the isentropic analyses, we identify that in P3, stronger convective updrafts take place in the high θ_{ei} regime where air parcels rarely reach. This is caused by reduced melting of rimed ice particles for energic parcels. Through defining convective core clouds, the relation between the convective structure on the isentropic diagram and the extreme precipitation can be identified. The shifts toward extreme intensity in the precipitation spectrum suggest that the microphysical processes have significant impacts on the extreme precipitation by the convective core clouds. The treatment of microphysics has significant impacts on the convective structures and then alter the probability of extreme events under the strongly forced environment.

Plain Language Summary

The microphysical parameterization typically represents cloud microphysical processes in the numerical models. In this study, the authors implemented a new parameterization (P3) in the model. The results show that extreme precipitation is more likely to occur when the environment is warm and moist compared with the original microphysics scheme. The change of the extreme precipitation is associated with the reduced melting effect in an ascending parcel. The melting of ice particles weakens the upward velocity of the parcel and then reduce the extreme

precipitation. P3 can reduce the melting effect by its ability to represent fast-falling hail particles, which can leave the parcel rapidly.

1 Introduction

Cloud microphysics plays an essential role in the cloud-resolving simulations of convective systems. Various simplifications are made in the representation of microphysical processes in the cloud-resolving models producing uncertainties of the simulated cloud structures and precipitation. Many studies have investigated these uncertainties through case-oriented (Tao et al. 2011; Morrison and Milbrandt 2011; Adams-Selin et al. 2013; Tao et al. 2016) or cumulus ensembles simulations (Grabowski et al.1999; Khairoutdinov and Randall 2003; Johnson et al. 2007). The former one access the overall performance of microphysics parameterizations for a specific real case or an idealized event. Tao et al. (2011) tested the performance of the Goddard microphysics parameterizations in simulating hurricane Katrina in the WRF model. The simulated hurricane is strongest in their study when they turned off the ice processes. Morrison and Milbrandt (2011) have illustrated that the choice of graupel as rimed ice led to a weaker cold pool and less precipitation compared to hail for an idealized supercell case. Adams-Selin et al. (2013) showed that the structure and the strength of an idealized convective system are sensitive to the predefined properties of graupel. Tao et al. (2016) improved the Goddard 4ICE scheme by revising formulations of ice processes, and the modified scheme showed better performances for continental squall cases. These studies suggest that ice processes are essential to the convective structures. The other approach is originally used to study convective variabilities in an idealized simulation with imposed large-scale destabilization and moisture source (Yanai 1973). Grabowski et al. (1999) pointed out that cloud microphysics can considerably affect mean temperature and moisture profiles, and its impacts should be evaluated in cumulus ensemble simulations. Khairoutdinov and Randall (2003) showed that the mean hydrometer profiles are sensitive to prescribed parameters. For instance, the increase of ice aggregation threshold leads

64 to more cloud ice in the upper atmosphere, and the increase of autoconversion and ice
65 aggregation rates resulted in less cloud water and cloud ice. Johnson et al. (2007) found that
66 convective precipitation became stronger within a narrow region when the ice microphysics is
67 eliminated. The above studies demonstrate the importance of adequately formulating ice-
68 processes in the cloud-resolving simulations of convective systems. In this study, we adopt the
69 cumulus ensemble approach.

70 The predicted particle properties scheme (P3, Morrison and Milbrandt 2015; Morrison et al.
71 2015; Mibrandt and Morrison 2016) has been implemented in the vector vorticity equation
72 cloud-resolving model (VVM, Jung and Arakawa 2008; Chien and Wu 2016; Wu et al. 2019) to
73 better represent the ice processes. In this study, we investigate the differences between the P3
74 scheme and the existing three-phase cloud microphysics parameterization (Lin 1983; Krueger et
75 al. 1995). We perform the idealized simulations with the large-scale forcing to obtain large
76 samples of strong convective systems and their overall statistics. instead of particular events
77 from the case-oriented simulations. Besides, we also use the isentropic analysis method (Pauluis
78 et al. 2013) to diagnose differences in convective structures. This method has been applied to
79 high-resolution model studies: moist convection (Pauluis et al. 2013; Pauluis 2016), hurricane
80 simulation (Mrowiec et al. 2016), and multiscale atmospheric overturning (Chen et al. 2018).
81 They took advantage of the ability of this technique to capturing the irreversible convective
82 overturning, and its ability is suitable for us to investigate convective responses of P3 and Lin.
83 The experiment setup and analysis method are described in section 2. Section 3 presents the
84 results of the comparison, and a summary and discussion are presented in section 4.
85

2 Materials and Methods

2.1 The model description

The vector vorticity equation cloud-resolving model (VVM) was developed by Jung and Arakawa (2008). The distinctive dynamical core is the adoption of the three-dimensional anelastic vorticity equations instead of the momentum equations. The velocity vectors are diagnosed through a three-dimensional elliptic equation and the vertical integrals of the vorticity. The use of the horizontal vorticities as prognostic variables removes the pressure gradient force in the governing equation. In this approach, the dynamics can respond to the thermal forcing directly. Therefore, the model can better represent the local-scale circulations due to a strong buoyancy gradient, such as land-sea breeze and cold pool fronts. The orographic effect is represented by implementing the immersed boundary method on the vorticity equation (Wu and Arakawa 2011; Chien and Wu 2016). The VVM is coupled with the Noah land surface model and the rapid radiative transfer model to more realistically simulate the interactions between convection, radiation, and land surface (Wu et al. 2019). This model has been used to study the unified parameterization for deep convection (Arakawa and Wu 2013; Wu and Arakawa 2014), stratocumulus transition (Tsai and Wu 2016), aggregated convection (Tsai and Wu 2017; Chen and Wu 2019), afternoon thunderstorms over complex topography (Kuo and Wu 2019; Wu et al. 2019), and the quasi-three-dimensional multiscale modeling framework (Jung and Arakawa 2016; Jung et al. 2019).

2.2 The experiment setup

Two experiments performed in this study share the same model setup except for the treatment of microphysics. Due to strong coupling with the dynamics, the direct impact of microphysical processes is difficult to evaluate (Grabowski 2014). Therefore, we impose strong and constant-

in-time large-scale forcing in the cyclic domain to reach the quasi-equilibrium state (Arakawa and Schubert 1974). In this case, the domain-averaged precipitation is strongly constrained by the large-scale forcing, and the impact of microphysical processes on the precipitation spectrum can be evaluated. Besides, the land surface and radiative processes are not applied to get rid of complicated interactions among these processes. The prescribed vertical profile of the forcing follows Arakawa and Wu (2013), which is chosen to counteract the apparent heat source and moisture sink typical of the Global Atmospheric Research Program (GARP) Atlantic Tropical Experiment (GATE) phase III after some idealization. The constant cooling rate of 2 K day^{-1} is also included to mimic radiative cooling. The simulations are initialized with the mean thermodynamic profiles from the GARP GATE phase III, and the background wind fields are nudged to calm state with a 2-hour time scale. The modeled domain is 512×512 km^2 with a 2 km resolution, and the vertical resolution stretches from 100 m at the bottom to roughly 1 km at the model top (20 km).

2.3 Microphysics schemes

The ice microphysics parameterizations used in this study are briefly introduced below. The original scheme (VVM-Lin) used in the VVM is a single-moment parameterization developed by Lin (1983), and some ice processes have been corrected by Krueger et al. (1995). The scheme separates ice-phase hydrometers into three predefined categories: cloud ice, snow, and graupel. The division of ice particles leads to the use of artificial parameters, such as the threshold or conversion rate between each category. Characteristics of the categories are prescribed, which causes discontinuous transition between ice species. On the other hand, the predicted particle properties scheme (P3) represents ice particles based on particle properties (Morrison and Milbrandt 2015; Morrison et al. 2015; Mibrandt and Morrison 2016). Four bulk ice properties,

total mass, total number, rimed mass, rimed volume, are used to allow four degrees of freedom within a single category. The approach evolves the ice properties continuously and avoids the use of artificial parameters. The P3 scheme has been tested by Morrison and Milbrandt (2015) and Morrison et al. (2015), and it can produce consistent results compared with other sophisticated two moment microphysics schemes and it is more computationally efficient. These two microphysics parameterizations are used in two simulations, respectively.

2.4 The isentropic analysis

The isentropic analysis method proposed by Pauluis et al. (2013) is used to diagnose differences in convection due to the microphysics in this study. The isentropic distribution is calculated through conditionally sampling according to the air parcel's equivalent potential temperature. The frozen equivalent potential temperature (Pauluis 2016), θ_{ei}, is used to include the latent heat of freezing, and its definition is

$$\left(C_{pd} + C_i r_T\right) \ln \frac{\theta_{ei}}{T_f} = \left[C_{pd} + r_i C_i + (r_v + r_l) C_l\right] \ln \frac{T}{T_f} - R_d \ln \frac{P_d}{P_0} + (r_v + r_l) \frac{L_f}{T_f} + r_v \frac{L_v}{T} - r_v R_v \ln \mathcal{H} \quad (1)$$

In the equation (1), C_{pd}, C_l, and C_i are the specific heat capacities at constant pressure of dry air, liquid water, and ice, respectively; r_T, r_v, r_l, and r_i are the mixing ratio of total water, water vapor, liquid water, and ice, respectively; L_v and L_f are the latent heat of vaporization and freezing, respectively; R_d and R_v are the specific gas constant of dry air and water vapor, respectively; P_0 is the reference pressure, 10^5 Pa; T_f is the freezing temperature of water, 273.15 K; and T is the temperature of air. The isentropic distribution of a given variable f is defined as

$$\langle f \rangle (z, \theta_{ei0}) = \frac{1}{P L_x L_y} \int_0^P \int_0^{L_y} \int_0^{L_x} f(x, y, z, t) \delta\left(\theta_{ei0}, \theta_{ei}(x, y, z, t)\right) dx dy dt \quad (2).$$

Here, P is the sampling period, and L_x, L_y are horizontal sampling length. δ is an approximate form of Dirac delta function,

$$\delta\left(\theta_{ei0}, \theta_{ei}(x,y,z,t)\right) = \begin{cases} 1/\Delta\theta_{ei}, & \theta_{ei0} - 0.5\Delta\theta_{ei} \le \theta_{ei} < \theta_{ei0} + 0.5\Delta\theta_{ei} \\ 0, & elsewhere \end{cases} \quad (3),$$

where θ_{ei} is the frozen equivalent potential temperature, and θ_{ei0} is the sampling reference, and $\Delta\theta_{ei}$ is the width of the finite bin. The mass-weighted isentropic mean of the variable,

$$\tilde{f}(z, \theta_{ei0}) = \frac{\langle \rho f \rangle (z, \theta_{ei0})}{\langle \rho \rangle (z, \theta_{ei0})} \quad (4),$$

is defined to approximate parcel's thermodynamic and dynamic properties on the isentropic coordinate. Reversible gravity oscillations are canceled out through this conditional sampling technique, and the irreversible convective overturning can be retained in the isentropic distribution. Warm, moist ascending air parcels are also separated from environmental subsidence. This method can provide the paths that a parcel would potentially undergo, and the parcel's properties can be estimated by isentropic mean technique. The isentropic analysis method allows us to compare our results based on thermodynamics and the parcel theory rather than complex flow structures.

3 Results

3.1 Vertical structure

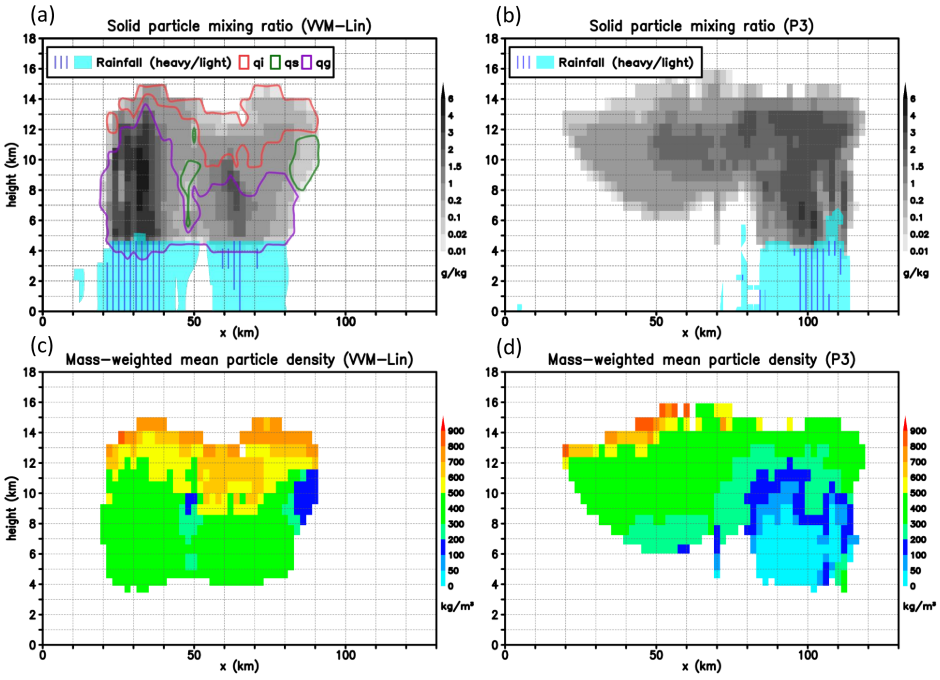

Fig. 1. The x-z cross-section of convection systems in VVM-Lin (a, c) and P3 (b, d) at t=12hr. Upper panels present the mixing ratio of solid particles (gray shading, g kg^{-1}) and rainy region (cyan shading and blue line). The color contours in (a) indicate the dominant ice specie which the mass faction of the specie is larger than 0.5. The mass-weighted mean particle density (kg m^{-3}) is showed in bottom panels.

The vertical cross-section of the simulated convective systems demonstrates differences in convective structures between the VVM-Lin and P3. The convective systems consist of the convective and stratiform regions visualized by the shading of the total ice mixing ratio (Fig. 1a and 1b). In the P3, the distribution of ice particles is diagnosed through four bulk ice properties. We can visualize the ice specie through the mass-weighted mean particle density (Fig. 1c and 1d). At the top of anvil cloud, the density is close to 917 km m^{-3}, which represents the less-rimed small ice particle. The density of the stratiform cloud is around 400 km m^{-3}, which represents the medium-rimed particle or the large aggregate. The very low density in the convective region suggests that there are heavy-rimed particles due to the convective updraft. In the VVM-Lin, the

178 total ice mixing ratio is the sum of all ice species: cloud ice, snow, and graupel. The cloud ice
179 mainly exists above 12 km, and the graupel is the dominant specie below 8 km (Fig. 1a). The
180 mass-weighted density (Fig. 1c) is the linear combination of predefined densities (cloud ice: 917
181 km m^{-3}, snow: 100 km m^{-3}, graupel: 400 km m^{-3}). The predefined densities change dramatically
182 from category to category, and this approach causes sharp change in the vertical structure. For
183 example, the density increases five times from snow-dominant region to cloud-ice-dominant
184 region at the edge of stratiform cloud (Fig. 1c). Below 8 km, the density is nearly constant in
185 graupel-dominant region. This result suggests that the VVM-Lin cannot represent the variability
186 of rimed ice particles in different regions in the convective systems. On the other hand, the P3
187 exhibits great variabilities between the convective and stratiform region with continuous density
188 distribution. The results show that the distribution and variability of the ice-phase particles are
189 better represented by the P3 scheme compared to the VVM-Lin.
190

191 ## 3.2 Convective statistics

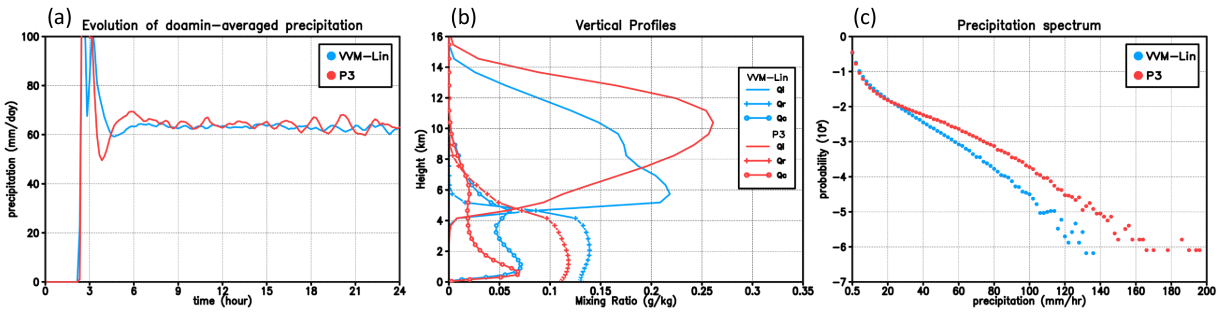

Fig. 2. (a) The time evolution of domain-averaged precipitation (mm hr^{-1}). (b) The mean vertical profiles (g kg^{-1}) of ice particles (Qi), rain water (Qr), and cloud water (Qc) within the last 12 hours. (c) The occurrence of precipitation is sampled with 2 mm hr^{-1} intervals on the intensity spectrum when the precipitation greater than 0.5 mm hr^{-1}.

192 It is well known that the interactions between the large-scale forcing and the response from
193 convective development remain quasi-equilibrium especially when the forcing is strong
194 (Arakawa 2004). The concept can be visualized by the time evolution of domain-averaged
195 precipitation in Fig. 2a. Despite the initial spin ups, the domain-averaged precipitation is similar
196 in both simulations with roughly 60 mm day^{-1}. We chose the last 12 hours as the simulations are
197 close to quasi-equilibrium to examine differences between two simulations. The domain-
198 averaged profiles of hydrometers are presented in Fig. 2b. The mixing ratio of ice is concentrated
199 at freezing level (~5 km) in the VVM-Lin (mainly contributed by the graupel), while a large
200 portion of ice in P3 exists in the upper layer (~10 km). On the other hand, the mixing ratios of
201 cloud water and rain water in the P3 are less than those in the VVM-Lin. The difference in liquid
202 water mixing ratio would influence the intensity distribution of precipitation even though the
203 domain-averaged precipitation is similar. This argument is supported by the precipitation
204 spectrum (Fig. 2c). The precipitation area is defined as a grid box where ten-minute precipitation
205 rate is larger than 0.5 mm hr^{-1}. The spectrum shows that the probability of precipitation
206 logarithmically decreases with the increase of the precipitation rate. The P3 exhibits higher

probability than the VVM-Lin when the precipitating rate is over 40 mm hr^{-1}. The differences become larger as the precipitation rate gets more extreme. The results show that the different treatment of ice microphysics processes can result in the change of precipitation spectrum under the constraint of quasi-equilibrium.

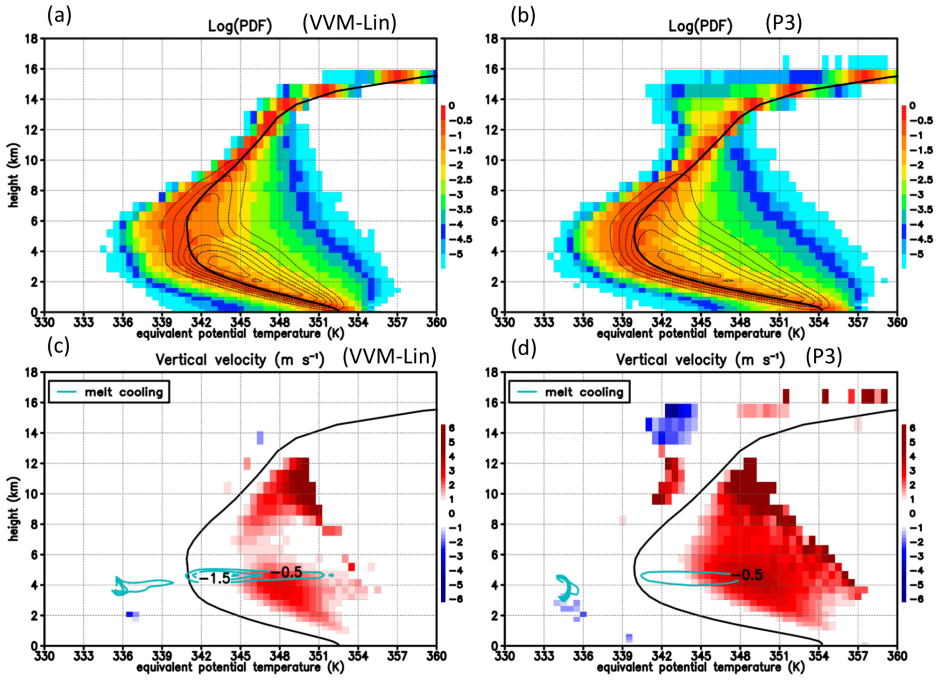

Fig. 3. The last 12 hr isentropic distributions of the VVM-Lin (a, c) and P3 (b, d). The probability density function of air parcels' frozen equivalent potential temperature (θ_{ei}) is presented by the color shading in upper panels. The isentropic convective stream function (kg m^{-2} s^{-1}) is presented as the contours with 0.01 kg m^{-2} s^{-1} interval. The isentropic-mean vertical velocity is showed as the color shading in bottom panels, and the cyan contours present the cooling rate of melting with 0.5 K hr^{-1}. The black lines are the mean θ_{ei} profiles within the sampling period.

The difference in precipitation spectrum would be associated with the change of convective structures. The cause of such difference is further analyzed through the isentropic distributions (Fig. 3). The probability density function for the VVM-Lin (Fig. 3a) and the P3 (Fig. 3b) is largest near the domain-averaged θ_{ei} profiles, and the distribution drops slowly toward high θ_{ei}. This distribution implies that most of area is covered by cold and dry subsidence, and moist convection occurs in narrow regions. The vertically tilt distributions to the mean θ_{ei} are collocated with the positive vertical velocity in the high θ_{ei} region (Fig. 3c and 3d). This tilting distributions of the isentropic-convective streamfunction could be used to approximate the path of ascending air parcels, so we simply call this region as isentropic-convective (IC) region. Air parcels in the P3 have stronger upward isentropic-mean vertical velocity in the IC region than

222 those in the VVM-Lin, especially in upper layer. In the VVM-Lin, the velocity distribution is
223 divided into two updraft regions in the lower and upper layer, while it continuously extends from
224 lower level to upper level in the P3. The ascending air parcels in the VVM-Lin slow down the
225 vertical velocity after entering freezing level (~5 km), but the parcels do not decelerate in the P3.
226 This difference in velocity distribution can be attributed to the variability of the rimed ice, and
227 the cyan contours in Fig. 3c and 3d represent the heating rate due to melting processes. The
228 VVM-Lin exhibits stronger cooling around the freezing level in the IC region. The predefined
229 graupel particles lead to concentrated cooling effect because of slow falling speed in the VVM-
230 Lin. On the other hand, P3 can represent hail-like and faster-falling particles, so the cooling is
231 weaker than that in the P3. The cold air entrains into warm parcels, and then reducing the
232 buoyancy and updraft. The stronger cooling effect causes the gap of vertical velocity in the
233 VVM-Lin. The inhibition of updraft does not take place, so there is stronger convective updraft
234 in the P3. The impact of ice variability on the convective structures is identified through the
235 isentropic analysis, and the change in the convective structures would alter the probability of the
236 extreme precipitation.
237

3.3 Convective core cloud analyses

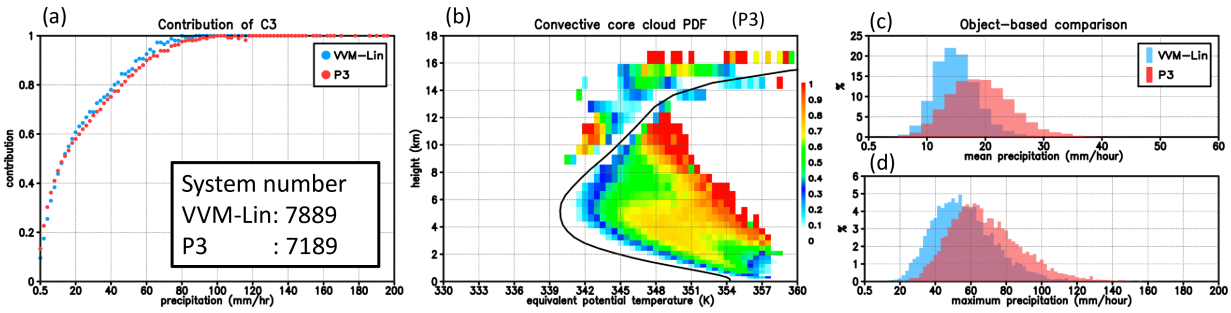

Fig. 4. (a) The fraction of precipitation grids covered by the surface projection of the convective core clouds. (b) The fraction of air parcels defined as the convective core cloud on the isentropic diagram. The right panel shows the probability of mean (c) and maximum (d) precipitation of each convective core cloud. The numbers of convective systems are, respectively, 7789 in the VVM-Lin and 7189 in the P3.

We identify the convective core cloud following Tsai and Wu (2017) to link the changes in convective structures and extreme precipitation. A cloudy grid is defined by the summation of all ice-phase species and cloud water greater than 10^{-5} kg kg^{-1} in this study, and contiguous cloudy grids are connected as a cloud object. The convective core cloud is selected by imposing additional criteria: the cloud base is lower than 2 km; the cloud top is higher than 6 km and the vertical velocity is greater than 0.5 m s^{-1}. The numbers of the convective core clouds in the VVM-Lin and the P3 are 7889 and 7189, respectively. The contribution of convective core clouds to the precipitation is defined as the fraction of precipitation grids covered by the projection to all precipitation grids. Fig. 4a shows that more than 80% of the precipitation greater than 40 mm hr^{-1} is contributed by the convective core clouds. The occurrence of the convective core clouds on the isentropic diagram is presented in Fig. 4b. The distribution of the fraction corresponds to the change due to microphysics processes in the IC region (Fig. 4b), so the differences in precipitation spectrum can be attributed to the changes of convective structures. We further analyze the spectrum of mean and maximum precipitation based on the convective

253 system. The system-based analysis shows that the convective core cloud tends to produce more
254 precipitation in the P3 (Fig. 4c). The P3 has a shift of the distribution toward more extreme
255 intensity in Fig. 4d. The ability to represent the different rimed ice between convective and
256 stratiform region enhance the extreme precipitation through the change in the convective
257 structures.
258

4 Conclusions

In this study, we implement the predicted particle properties (P3) scheme and examine its impact on precipitation spectrum compared to the original VVM-Lin scheme. Two idealized simulations are performed by using the vector vorticity equation cloud- resolving model (VVM). Strong large-scale forcing is imposed in the cyclic do main to constrain the domain-averaged precipitation to obtain large samples of strong convective systems. The P3 exhibits a higher variation of the ice particles with a single category; for example, heavy-rimed particles in the convective updraft and large aggregates in the stratiform region. In the VVM-Lin, the use of graupel as the rimed ice species results in the monotonous feature of the ice particles in a different region. The impacts of the different representation of the rimed ice particles on the convective structures are investigated by the isentropic analyses. The melting of the rimed particles results in the cooling in the convective updraft. The cooling effect is stronger in the convective region in the VVM-Lin due to slower falling speed of the graupel and therefore the weakening of the convective updraft. On the other hand, the P3 can produce fast-falling hail-like particles in the convective region, so the convective updraft is not inhibited by the cooling effect. The change of convective structures is identified as the main reason for the shift in the precipitation spectrum through the convective core cloud analyses. The more realistic representation of the ice particles reduces the cooling effect and results in more extreme precipitation in the P3.

This study demonstrates the role of convective structure change in connecting microphysical processes and extreme precipitation. Detailed microphysical effects modify the statistics of the convective structure leading to the change of the precipitation spectrum. In the future, the interactions among all other physical processes, such as radiation, turbulence, and boundary

layer processes, can be evaluated using similar concepts. Depending on the process of interest, the specific experimental setup can be different. For example, the cloud-radiation interaction can be evaluated in the radiative-convective-equilibrium (RCE) simulations. The convective structure changes due to microphysical processes can interact with the radiation leading to a different stage of convective aggregation. In this approach, we can compare the statistics of convective structure among various cloud-resolving simulations to understand the impacts of the specific physical processes.

Acknowledgments

We thank the editor and reviewers for providing insightful comments that led to the improvement of the manuscript. We also thank Dr. Morrison for providing valuable discussions on the manuscript. The model results of VVM used in this study can be downloaded online (from https://doi.org/10.6084/m9.figshare.11933148.v1). The authors are supported by Taiwan's MoST through Grant 107-2111-M-002-010-MY4 to National Taiwan University.

296 **References**

297 Adams-Selin, R. D., van den Heever, S. C., & Johnson, R. H. (2013). Impacts of graupel
298 parameterization schemes on idealized bow echo simulations. Monthly Weather Review,
299 141, 3735–3756. https://doi.org/10.1175/MWR-D-12-00343.1

300 Arakawa, A. (2004). The cumulus parameterization problem: Past, present, and future. Journal of
301 Climate, 17, 2493–2525. https://doi.org/10.1175/1520-
302 0442(2004)017<2493:RATCPP>2.0.CO;2

303 Arakawa, A., & Schubert, W. H. (1974). Interaction of a cumulus cloud ensemble with large-
304 scale environment, Part I. Journal of the Atmospheric Sciences, 31(3), 674–701.
305 https://doi.org/10.1175/1520-0469(1974)031<0674:IOACCE>2.0.CO;2

306 Arakawa, A., & Wu, C.-M. (2013). A unified representation of deep moist convection in
307 numerical modeling of the atmosphere. Part I. Journal of the Atmospheric Sciences,
308 70(7), 1977–1992. https://doi.org/10.1175/JAS-D-12-0330.1

309 Chen, X., Pauluis, O. M., Leung, L. R., & Zhang, F. (2018). Multiscale Atmospheric
310 Overturning of the Indian Summer Monsoon as Seen through Isentropic Analysis. Journal
311 of the Atmospheric Sciences, 75, 3011–3030. https://doi.org/10.1175/JAS-D-18-0068.1

312 Chen, Y.-T., & Wu, C.-M. (2019). The role of interactive SST in the cloud-resolving simulations
313 of aggregated convection. Journal of Advances in Modeling Earth Systems, 11, 3321–
314 3340. https://doi.org/10.1029/2019MS001762

315 Chien, M.-H., & Wu, C.-M. (2016). Representation of topography by partial steps using the
316 immersed boundary method in a vector vorticity equation model (VVM). Journal of

317 Advances in Modeling Earth Systems, 8, 212–223.
318 https://doi.org/10.1002/2015MS000514

319 Grabowski, W. W. (2014). Extracting microphysical impacts in large-eddy simulations of
320 shallow convection. Journal of the Atmospheric Sciences, 71, 4493–4499.
321 https://doi.org/10.1175/JAS-D-14-0231.1

322 Grabowski, W. W., Wu, X., & Moncrieff, M. W. (1999). Cloud resolving modeling of tropical
323 cloud systems during phase III of GATE. Part III: Effects of cloud microphysics. Journal
324 of the Atmospheric Sciences, 56, 2384–2402. https://doi.org/10.1175/1520-
325 0469(1999)056<2384:CRMOTC>2.0.CO;2

326 Johnson, D. E., Tao, W.-K., & Simpson, J. (2007). A study of the response of deep tropical
327 clouds to large-scale thermodynamic forcings. Part II: Sensitivities to microphysics,
328 radiation and surface fluxes. Journal of the Atmospheric Sciences, 64, 869–886.
329 https://doi.org/10.1175/JAS3846.1

330 Jung, J.-H., & Arakawa, A. (2008). A three-dimensional anelastic model based on the vorticity
331 equation. Monthly Weather Review., 136(1), 276–294.
332 https://doi.org/10.1175/2007MWR2095.1

333 Jung, J.-H., & Arakawa, A. (2016). Simulation of subgrid orographic precipitation with an
334 embedded 2-D cloud-resolving model. Journal of Advances in Modeling Earth Systems,
335 8, 31–40. https://doi.org/10.1002/2015MS000539

336 Jung, J.-H., Konor, C. S., & Randall, D. (2019). Implementation of the vector vorticity
337 dynamical core on cubed sphere for use in the Quasi-3-D Multiscale Modeling

Framework. Journal of Advances in Modeling Earth Systems, 11, 560–577. https://doi.org/10.1029/2018MS001517

Khairoutdinov, M. F., & Randall, D. A. (2003). Cloud resolving modeling of the ARM summer 1997 IOP: Model formulation, results, uncertainties, and sensitivities. Journal of the Atmospheric Sciences, 60, 607–625. https://doi.org/10.1175/1520-0469(2003)060,0607:CRMOTA.2.0.CO;2

Krueger, S. K., Fu, Q., Liou, K., & Chin, H.-N. S. (1995). Improvements of an ice-phase microphysics parameterization for use in numerical simulations of tropical convection. Journal of Applied Meteorology, 34(1), 281–287. https://doi.org/10.1175/1520-0450-34.1.281

Kuo, K.-T., & Wu, C.-M. (2019). The precipitation hotspots of afternoon thunderstorms over the Taipei Basin: Idealized numerical simulations. Journal of the Meteorological Society of Japan, 97, 501–517. https://doi.org/10.2151/jmsj.2019-031

Lin, Y.-L., Farley, R. D., & Orville, H. D. (1983). Bulk parameterization of the snow field in a cloud model. Journal of Climate and Applied Meteorology, 22, 1065–1092. https://doi.org/10.1175/1520-0450(1983)022<1065:BPOTSF>2.0.CO;2

Milbrandt, J. A., & Morrison, H. (2016). Parameterization of cloud microphysics based on the prediction of bulk ice particle properties. Part III: Introduction of multiple free categories. Journal of the Atmospheric Sciences, 73, 975–995. https://doi.org/10.1175/JAS-D-15-0204.1

Morrison, H., & Milbrandt, J. A. (2011). Comparison of two-moment bulk microphysics schemes in idealized supercell thunderstorm simulations. Monthly Weather Review, 139, 1103–1130. https://doi.org/10.1175/2010MWR3433.1

Morrison, H., & Milbrandt, J. A. (2015). Parameterization of ice microphysics based on the prediction of bulk particle properties. Part I: Scheme description and idealized tests. Journal of the Atmospheric Sciences, 72, 287–311. https://doi.org/10.1175/JAS-D-14-0065.1

Morrison, H., Milbrandt, J. A., Bryan, G. H., Ikeda, K., Tessendorf, S. A., & Thompson, G. (2015). Parameterization of cloud microphysics based on the prediction of bulk ice particle properties. Part II: Case study comparisons with observations and other schemes. Journal of the Atmospheric Sciences, 72, 312–339. https://doi.org/10.1175/JAS-D-14-0066.1

Mrowiec, A. A., Pauluis, O. M., & Zhang, F. (2016). Isentropic analysis of a simulated hurricane. Journal of the Atmospheric Sciences, 73, 1857–1870. https://doi.org/10.1175/JAS-D-15-0063.1

Pauluis, O., & Mrowiec, A. A. (2013). Isentropic analysis of convective motions. Journal of the Atmospheric Sciences, 70, 3673–3688. https://doi.org/10.1175/JAS-D-12-0205.1

Pauluis, O. (2016). The mean air flow as Lagrangian dynamics approximation and its application to moist convection. Journal of the Atmospheric Sciences, 73, 4407–4425. https://doi.org/10.1175/JAS-D-15-0284.1

Tao, W.-K., Shi, J. J., Chen, S. S., Lang, S., Lin, P.-L., Hong, S.-Y., Peters-Lidard, C., & Hou, A. (2011). The impact of microphysical schemes on hurricane intensity and track. Asia-

Pacific Journal of Atmospheric Sciences, 47(1), 1–16. https://doi.org/10.1007/s13143-011-1001-z

Tao, W.-K., Wu, D., Lang, S., Chern, J.-D., Peters-Lidard, C., Fridlind, A., & Matsui, T. (2016). High-resolution NU-WRF simulations of a deep convective-precipitation system during MC3E: Further improvements and comparisons between Goddard microphysics schemes and observations, Journal of Geophysical Research: Atmospheres, 121, 1278–305. https://doi.org/10.1002/2015JD023986.

Tsai, J.-Y., & Wu, C.-M. (2016). Critical transitions of stratocumulus dynamical systems due to perturbation in free atmosphere moisture. Dynamics of Atmospheres and Oceans, 76, 1–13. https://doi.org/10.1016/j.dynatmoce.2016.08.002

Tsai, W.-M., & Wu, C.-M. (2017). The environment of aggregated deep convection. Journal of Advances in Modeling Earth Systems, 9, 2061–2078, https://doi.org/10.1002/2017MS000967.

Wu, C.-M., & Arakawa, A. (2011). Inclusion of surface topography into the vector vorticity equation model (VVM). Journal of Advances in Modeling Earth Systems, 3, M04002. https://doi.org/10.1029/2011MS000061

Wu, C.-M., & Arakawa, A. (2014). A unified representation of deep moist convection in numerical modeling of the atmosphere. Part II. Journal of the Atmospheric Sciences, 71(6), 2089–2103. https://doi.org/10.1175/JAS-D-13-0382.1

Wu, C.-M., Lin, H.-C., Cheng, F.-Y., & Chien, M.-H. (2019). Implementation of the land surface processes into a vector vorticity equation model (VVM) to study its impact on afternoon

401 thunderstorms over complex topography in Taiwan. Asia-Pacific Journal of Atmospheric
402 Sciences. https://doi.org/10.1007/s13143-019-00116-x

403 Yanai, M., Esbensen, S., & Chu, J.-H. (1973). Determination of bulk properties of tropical cloud
404 clusters from large-scale heat and moisture budgets. Journal of the Atmospheric Sciences,
405 30, 611–627. https://doi.org/10.1175/1520-0469(1973)030,0611:DOBPOT.2.0.CO;2